IEEE Access
Multidisciplinary | Rapid Review | Open Access Journal

Received November 25, 2021, accepted December 26, 2021, date of publication January 6, 2022, date of current version January 20, 2022.

Digital Object Identifier 10.1109/ACCESS.2021.3140103

A Statistical Shape-Based Patient-Specific Anatomical Structure Model

ZHUYE XU[1] AND XIAOQIANG ZHAO[2,3]

[1]School of New Energy and Power Engineering, Lanzhou Jiaotong University, Lanzhou 730070, China
[2]College of Electrical and Information Engineering, Lanzhou University of Technology, Lanzhou 730050, China
[3]Key Laboratory of Gansu Advanced Control for Industrial Process, Lanzhou University of Technology, Lanzhou 730050, China

Corresponding author: Xiaoqiang Zhao (xqzhao@lut.edu.cn)

This work was supported in part by the Project funded by the Open Fund of the State Key Laboratory of Large Electric Drive System and Equipment Technology under Grant SKLLDJ012016020, in part by the National Natural Science Foundation of China under Grant 61763029, in part by the Open Fund Project of the Key Laboratory of Gansu Advanced Control for Industrial Process under Grant 2019KFJJ01, and in part by the Young Scholars Science Foundation of Lanzhou Jiaotong University under Grant 2021032.

ABSTRACT A patient-specific anatomical structure model has been widely used in many medical applications. However, in practical applications, to effectively construct a patient-specific anatomical structure model is a challenge, the reasons are: 1) the manual marking process for landmark points is time-consuming and is prone to have false points; 2) the correspondence establishment is difficult; and 3) the performance of the model is limited. Therefore, the purpose of this study is to automatically construct a patient-specific anatomical structure model to solve these difficulties. Firstly, the input data are preprocessed to enhance the region of interest in CT scan images. Then, the region of interest is regarded as a training specimen, and the triangle is used to mesh the training specimen. Meanwhile, vertices contraction strategy is introduced to iteratively contract triangle meshes, and the correspondences are established through improved B-spline free-form deformation. Finally, principal component analysis is used to generate the final patient-specific anatomical structure model. Experimental results on 30 pelvic CT scan images verify that the proposed method outperforms the compared methods.

INDEX TERMS Medical image processing, shape analysis, statistical shape model, vertices contraction, B-spline free-form deformation.

I. INTRODUCTION

A. BACKGROUNDS

The construction of patient-specific anatomical structure model [1] from shape population based on statistical shape [2] has been widely used in medical image processing fields, such as computer-aided diagnosis [3], modeling of keen biomechanics [4], facial defects reconstruction [5], surgical planning and navigation [6]–[8]. An anatomical structure model effectively visualizes and provides on-demand information from 3D data, such as Computed Tomography (CT) [9] and Magnetic Resonance Imaging (MRI) [10]. It can help doctors diagnose accurately and conduct proper subsequent treatments. However, the traditional methods for the anatomical structure model have several problems: (1) they require manual selection of landmark points and thus have lower accuracy. (2) the correspondence between the template specimen and the target specimens is difficult. (3) the accuracy of the constructed model is limited.

The associate editor coordinating the review of this manuscript and approving it for publication was Rajeswari Sundararajan.

B. PREVIOUS STUDIES

In order to solve these problems, some previous studies have proposed many methods to construct the patient-specific anatomical structure model. Kelemen *et al.*. [11] proposed the Spherical Harmonics Descriptors Method (SPHARM), which defined the parameterized correspondence of the spherical harmonic function in each target shape. By seeking a mapping from surfaces to spheres, an anatomical model was constructed on a set of closed 3D surfaces. SPHARM effectively established the correspondence between the template specimen and the target specimens, but the constructed model only was applicable to spheres. To overcome this problem, Davies *et al.*. [12] proposed Minimum Description Length (MDL) method based on a novel objective function. In MDL, the correspondence relationship was represented by using the minimum description length criterion. MDL

was not only applicable to spheres, but also applicable to non-spherical training dataset. However, the accuracy of the model constructed by MDL was not high, and the process of calculating the minimum length was more complicated. So Davies [13] proposed a statistical shape model (SSM) for the patient anatomical structure, where landmark points were manually marked and used to establish the correspondence. The computational accuracy was effectively improved by introducing the statistical shape model, and the computational process was relatively simple. However, in the phase of model construction, it was necessary to manually mark the position of each landmark point. This process was time-consuming and prone to the operator's error. Consequently, Dalal *et al.*. [14] developed the Landmark Sliding Method (SLIDE) to automatically mark landmark points. In SLIDE, target shapes were aligned to template shape, and the initial correspondence of the landmark points was evaluated based on Euclidean distance. Then, the landmark points were iteratively slid along the tangent planes of the landmark points to minimize the shape deformation and shape representation error. SLIDE could construct an anatomical structure model. However, it was necessary to continuously calculate the tangent planes of each landmark point during the sliding process. The process was complicated and only applicable to an image with a little number of landmark points. Based on the previous methods, Barratt *et al.*. [15] conducted a comprehensive analysis of the statistical shape model to construct a patient-specific anatomical structure model. A novel method was developed to construct a statistical shape model of the femur and pelvis through 3D ultrasound imaging. They represented the template bone surface with triangular mesh and registered the template to the UltraSound (US) surface point cloud through the iterative nearest neighbor method. Thereafter, the weight parameters corresponding to the first five principal modes are optimized. This method showed potential for facilitating image-guided orthopedic surgery without the expense and radiation dose associated with a preoperative CT scan. Eck *et al.*. [16] used a 3D intensity model based on spherical harmonics to analyze the shape and intensity of the heterochromatin focus. It fitted the statistical model to the image intensity model to determine the final model parameters. In order to demonstrate that the statistical shape model could be considered a successful tool to support surgeons in the preoperative planning of glenoid, Abler *et al.*. [17] used a statistical shape model constructed from 64 healthy scapulae to reconstruct the premorbid glenoid shape. They validated on healthy scapulae by quantifying the accuracy of the predicted shape in terms of surface distance, glenoid version and inclination. This method could quantify the accuracy of SSM-based predictions on a population by comparing the glenoid cavity predicted with the actual 3D glenoid anatomy. To further investigate the performance of the patient-specific anatomical structure model constructed with SSM, Plessers *et al.*. [18] proposed a novel method to assess the performance of an SSM-based reconstruction method on glenoid bone reconstruction and anatomic parameter prediction. The inclination, version and glenoid center points of the reconstructed surface were compared with the original parameters of each scapula. This method showed that an SSM enabled accurate reconstruction of a glenoid bone defect and prediction of native anatomic parameters. Gao *et al.*. [19] developed a fully automatic method to segment the three-dimensional coronary from computed tomography angiography (CTA) image data. Coronary borders from the 2D planes could be extracted by projecting the cross-sectional CTA images to eight directions, and according to the intersection between the aorta and coronary, the location of the coronary root was determined. Compared with other methods, this method applied the dynamic programming to directly extract the vessel wall, and it could effectively segment three-dimensional coronary from image data and obtained better accuracy, thus a powerful basis for the subsequent coronary analysis was obtained.

Generally speaking, common mesh simplification methods include Marching Cubes Edge Collapse (MCEC) and Quadric Edge Collapse Decimation (QECD). MCEC is a mesh simplification method based on Marching Cubes (MC). It can minimize the number of triangle vertices in the target specimen, and the speed of meshing is relatively fast. However, MCEC is prone to distortion when the structure of the target specimen is complex. QECD is a mesh simplification method based on edge collapse. The essence of QECD is to collapse the edges with smaller changes in the mesh, and introduce a cost function to make the edges possess smaller cost. The disadvantage of QECD is that the number of reduced triangles is relatively small, and the speed of meshing is relatively slow.

C. CONTRIBUTION AND INNOVATIONS OF OUR METHOD

The contribution of this paper is to propose a comprehensive method to construct a patient-specific anatomical structure model. After adopting this comprehensive method, we can construct model with better performance. The process of constructing the model mainly includes the following two innovations. An innovation point is to propose a vertices contraction strategy to conduct mesh simplification. This strategy can effectively reduce the number of mesh vertices and the complexity of computational in the phase of model construction. And the experiment result show that vertices contraction can effectively reduce the vertices number compared with MCEC and QECD. Another innovation point is to propose an improved B-spline free form deformation to successful establish the correspondence. Through the improved b-spline free form deformation, we get the mapping of each control point and concatenate all the control points to get the mapping between the template specimen and the target specimens.

II. THE PROPOSED METHOD

The proposed method constructs a patient-specific anatomical structure model and provides a basis for doctors to

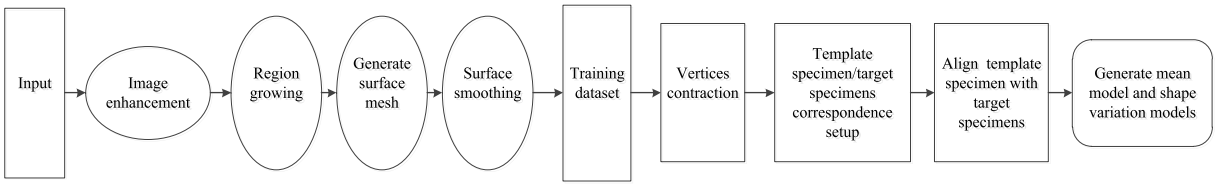

FIGURE 1. The schematic diagram of our method.

analyze the patient's conditions. Different doctors are good at interpreting different patient information when patients are in the hospital. Generally speaking, the conditions of patient information mainly include numerical information such as blood test and urine test, image information such as scanned images, sequence information such as electrocardiogram, and text information on electronic medical records. Part of the patient information can be obtained through inquiries, and part of the information needs to be obtained through a physical examination, which reflects the complexity of patient information. The patient's conditions mentioned in this paper refers to analyzing the patient's image information, and constructing a corresponding 3D model based on the image information. In addition, the application condition of the method in this paper is CT/MRI image. We model the slices of these images to construct the patient's anatomical structure. The ''patient-specific anatomical structural model'' means that we reconstruct the 3D geometric model of a patient with the statistical shape model based on the training dataset. The schematic diagram of our method is shown in Figure 1. The image enhancement step is to remove the noise in the image, so that the region of interest in the target image is more prominent and the segmentation results can be more accurate.

A. DATA PROCESSING

Pre-processing methods are applied to CT images to enhance the region of interest. First, the region of interest is extracted from the CT images by using the region growing method [20]. Then, the Marching Cubes method [21] is employed to generate a surface mesh while the inter-slicer connectivity is maintained. Finally, a mean filter is applied to each region of interest to reduce noise. The pre-processed regions of interest are used as training data for subsequent modeling.

B. VERTICES CONTRACTION

First, a template specimen is selected from training data $\Omega = \{S_1, S_2, \cdots S_N\}$, where N is the number of images. The selected template specimen S_1 is visualized and meshed with triangles. Because constructing the correspondence between the template and target specimens is time-consuming, the vertices contraction strategy is employed. The strategy effectively reduces the number of vertices while the distortion of specimens is avoided. Let V_a denote vertices of the specimen S_1, $(V_a, V_b) \rightarrow V_\beta$ indicates that the pair of vertices V_a and V_b moves to the new position V_β, where V_β connected all their incident edges to V_a and V_b is removed. (V_a, V_b) can

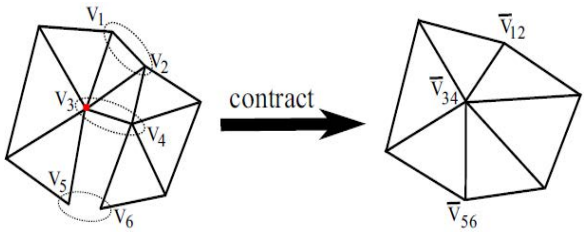

FIGURE 2. The vertices contraction process.

be either an edge or two non-connected vertices under some conditions. Through this process, we can contract a series of vertices into a single vertex $(V_1, V_2, V_3, \cdots V_k) \rightarrow V_\beta$. The vertices contraction process is depicted in Figure 2.

As shown in Figure 2, we can see that the point pair (V_1, V_2) becomes a new vertex $\bar{V}_{12}$ through vertices contraction, and the vertex V_2 is deleted, the point pair (V_3, V_4) becomes a new vertex $\bar{V}_{34}$ through vertices contraction, the point pair (V_5, V_6) becomes a new vertex $\bar{V}_{56}$ through vertices contraction. The number of vertices is effectively reduced after vertices contraction is used. Furthermore, to avoid the distortion of training specimens, the following constraints are employed on (V_a, V_b):

(1) V_a is not a special vertex. Generally speaking, the special vertex means that we need to manually specify some vertices in advance in the phase of vertices contraction. And then perform vertices contraction on other vertices. And the criteria of choosing special vertex is the position of this vertex could not change during the vertices contraction. Such point is called special vertex, such as V_3 in Figure 2.

(2) (V_a, V_b) is an edge;

(3) $\| V_a - V_b \| < t$, where t is a threshold.

The vertices contraction is applied to all images in training data Ω.

C. CORRESPONDENCE ESTABLISHMENT

After S_1 has performed vertices contraction, we also perform vertices contraction on the remaining specimens $\{S_2, S_3 \ldots S_N\}$ in training data Ω, and S_2 is selected as the target specimen after vertices contraction. In the process of constructing a patient-specific anatomical structure model, we register S_1 to $\{S_2, S_3 \ldots S_N\}$ respectively and establish the correspondence. Registration S_1 to S_2 means that a mapping is searched between the template specimen S_1 and the target specimen S_2, and this mapping describes semantically the position relationship between points. We introduce improved B-spline free-form deformation to register S_1 to S_2. Under

the assumption that S_1 and S_2 have L landmark points, S_1 is transformed into S_2 by mapping ϕ which is defined as follows:

$$\phi(u) = \sum_{i \in L} P_i B_i(u) \tag{1}$$

where P_i represents the $i-th$ landmark point, B_i is the basis of B-spline corresponding to P_i, $u \in [0,1]^d$ is the parameter value, and $d = 2, 3$ is the dimension of Euclidean space.

Both S_1 and S_2 are composed of mesh, and the mesh is composed of landmark points, so we regard the landmark point P_i as control point. We assume that the coordinate of the control point is $\{x, y, z\}$, and the control point P_i can be expressed as $P_{x,y,z}$. Equation (1) is a general expression of the mapping from S_1 to S_2. We extend equation (1) in the form of coordinates, as shown in equation (2):

$$\phi(S_1) = \sum_{h=0}^{3}\sum_{g=0}^{3}\sum_{t=0}^{3} B_h(u) B_g(v) B_t(w) P_{x+h,y+g,z+t} \tag{2}$$

where $B_h(u)$ denotes the $h-th$ basis function of the b-spline, and the parameter is u. Similarly, $B_g(v)$ denotes the $g-th$ basis function of the b-spline, the parameter is v, $B_t(w)$ denotes the $t-th$ basis function of the b-spline, the parameter is w. h, g and t denote the base coordinates of the b-spline corresponding to $\{x, y, z\}$.

$$B_0(u) = \frac{(1-u)^3}{6} \tag{3}$$

$$B_1(u) = \frac{\left(3u^3 - 6u^2 + 4\right)}{6} \tag{4}$$

$$B_2(u) = \frac{\left(-3u^3 + 3u^2 + 3u + 1\right)}{6} \tag{5}$$

$$B_3(u) = \frac{u^3}{6} \tag{6}$$

So we can get the mapping of each control point. Thereafter, we concatenate the mapping of each control point to get the mapping of S_1.

The registration is achieved by minimizing equation (7):

$$Min\left(\omega_{deviation} + \lambda\omega_{smooth} + \mu\omega_{landmarks}\right) \tag{7}$$

where $\omega_{deviation}$ represents the sum of squared deviations between the deformed template specimen $\phi(S_1)$ and the target specimen S_2.

$$\omega_{deviation} = \sum \left\| \phi\left(v_j^{(1)}\right) - v_j^{(2,c)} \right\|^2 \tag{8}$$

where ϕ is the mapping defined by equation (1), $v_j^{(1)}$ is a vertex in S_1, and $v_j^{(2,c)}$ is the closest vertex of $v_j^{(1)}$ in S_2. And ω_{smooth} represents the smoothness between the S_1 and S_2. ω_{smooth} in equation (7) is the smoothness term defined as follows:

$$\omega_{smooth} = \int_{S_1,S_2} \left\| \left(\sum_1^d \frac{\partial}{\partial x} \right)^2 \phi \right\|^2 dx \tag{9}$$

$\omega_{landmarks}$ in equation (7) denotes the matching error of the landmark points between the template and target specimens.

$$\omega_{landmarks} = \sum_{j=1}^{L} \left\| \phi\left(\bar{v}_j^{(1)}\right) - \bar{v}_j^{(2)} \right\|^2 \tag{10}$$

$\left\{\left(\bar{v}_1^{(1)}, \bar{v}_1^{(2)}\right), \ldots \left(\bar{v}_L^{(1)}, \bar{v}_L^{(2)}\right)\right\}$ are the pairs of landmark points of S_1 and S_2. The coefficients λ and μ control the weights for ω_{smooth} and $\omega_{landmarks}$, respectively. The initial value λ is set to a large value and then gradually reduces.

We adopt the typical optimal method [22] to minimize equation (7) and compute the mapping in equation (1). The deformed template specimen $\phi(S_1)$ is projected onto the target specimen S_2 along the direction of the vertex normal to establish the correspondence between the template specimen S_1 and the target specimen S_2. Note that all the correspondences from S_1 to $\{S_3, S_4 \ldots S_N\}$ are also computed. Then, S_1 is aligned with other specimens via Procrustes analysis [23], and the effects of the specimen are eliminated due to rotation and scale changes.

D. PRINCIPAL COMPONENT ANALYSIS

When the correspondence between the template specimen S_1 and the target specimen S_2 is successfully established, we use the same steps to establish correspondence between S_1 and $\{S_3, S_4 \ldots S_N\}$, respectively. After that, a normal distribution is used to represent the shape change of the patient-specific anatomical structure model s as follows:

$$s \sim \theta(\bar{s}, C) \tag{11}$$

$$\bar{s} = \frac{1}{N}\sum_{n=1}^{N} S_n \tag{12}$$

$$C = \frac{1}{N-1}\sum_{n=1}^{N} (S_n - \bar{s})(S_n - \bar{s})^T \tag{13}$$

where $\bar{s}$ denotes the mean shape and C denotes the covariance matrix. Finally, principal component analysis is used to generate the final expression of the patient-specific anatomical structure model. The general expression is the sum of the mean shape and the main deformation models as follows:

$$s = \bar{s} + \sum_{m=1}^{M} u_m e_m \tag{14}$$

where M is the number of main deformation modes. u_m and e_m represent the mth eigenvalue and eigenvector, respectively. The eigenvectors are sorted in descending order, they satisfy:

$$u_m > u_{m+1} \tag{15}$$

When u_m decays rapidly, s can be accurately approximated by the first G principal components of the deformation modes:

$$s = \bar{s} + \sum_{m=1}^{G} u_m e_m \tag{16}$$

G is selected by equation (17):

$$\frac{\sum_{m=1}^{G} u_m}{\sum_{m=1}^{M} u_m} \geq P \tag{17}$$

where P is the percentage of the whole deformed models that we want the first G principal components to represent.

III. EXPERIMENTAL VERIFICATION

The performance of the proposed method is compared with the other methods on 30 pelvic CT scan images. Firstly, specimens are selected with landmark points of 738, 512, and 356 to construct patient-specific anatomical structure models. Then, suitable specimen points are selected through compactness, specificity, generality and representation of the model.

Compactness [24] represents the model ability which describes the deformed model with as few principal components as possible. It is defined as the cumulative sum of the eigenvalues corresponding to the deformed model. Specificity [25] measures the ability of the model to generate instances similar to those available within the training set. It is defined as the average fitting error between the created shape instance and the most similar shape instance in the training data. Generality [26] is the ability to generate instances not explicitly provided by the training data. It is defined that leaves one specimen out in the training data, and then a model with the remaining specimens in the training data is constructed and a fit error is found between the constructed model and the leaved out specimen. Representation is measured by the average distance from each point in the shape to the landmark point. Note that the smaller values of these four indicators mean better model performance.

A. USABILITY EVALUATION

In order to verify the usability of the proposed method, the 30 pelvic 3D CT scan images are used. The CT resolution is 0.9mm on the plane and 1.5mm between slices. The left femur region of the pelvis is the region of interest. By processing the pelvic CT scan images, we obtain 30 left femur images and regard them as training data. To observe the training data more intuitively, we place 30 left femur images in a plane as shown in Figure 3.

Table 1 shows the anthropometry and demographics information of the training data $\Omega = \{S_1, S_2, \cdots S_N\}$ where N is 30. A femur image 001 in the training data Ω is randomly selected as template specimen S_1. Figure 4 shows the visualization results where color bars represent the color changes of the image under different saturation. The meshed form of S_1 with triangles is defined as S_1' and visualized in Figure 5.

The numbers of triangle surfaces and vertices of S_1' are 102,080 and 51,042, respectively. Also, all femur images in Ω are meshed with triangles. The numbers of vertices of the meshed femur image are between 4,432 and 78,176. The numbers of triangle surfaces are between 8,840 and 156,348, as shown in Table 1.

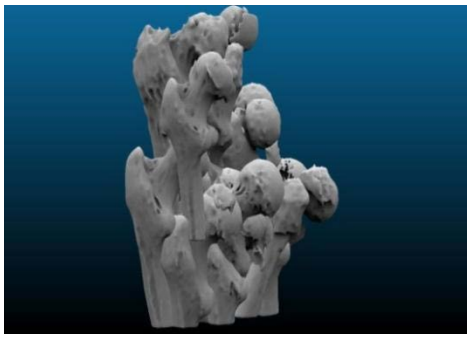

FIGURE 3. 30 left femur images in a plane.

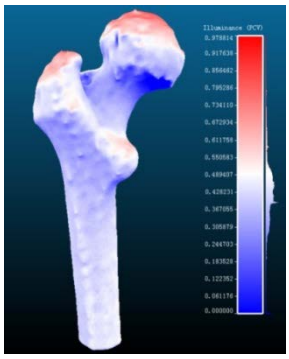

FIGURE 4. Visualization of S_1.

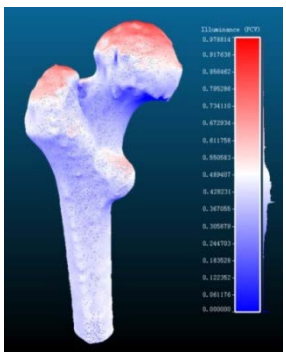

FIGURE 5. Visualization of S_1'.

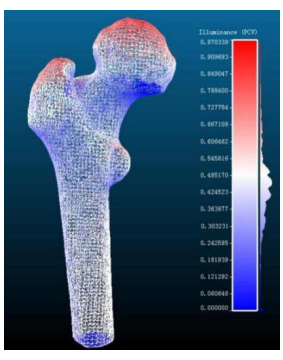

FIGURE 6. Visualization of S_1''.

TABLE 1. Anthropometry and demographics information of 30 left femur images.

ID	Age(Year)	Sex	Weight(Kg)	Height(cm)	Faces(Number)	Vertices(Number)
001	25	Male	61	175	102080	51042
002	29	Male	72	180	98744	49370
003	32	Male	70	167	87876	43940
004	26	Male	66	165	109528	54752
005	26	Male	63	170	112800	56410
006	29	Male	80	180	106268	53130
007	30	Male	83	176	156348	78176
008	35	Male	79	175	117744	58876
009	32	Male	75	170	97116	48560
010	32	Male	80	168	76204	38110
011	27	Male	62	166	114452	57224
012	26	Male	60	181	99548	49770
013	30	Male	80	182	95536	47760
014	33	Male	83	178	99512	49746
015	30	Male	85	179	92184	46084
016	42	Female	65	159	95432	47708
017	40	Female	62	158	88288	44140
018	41	Female	62	162	56244	28120
019	36	Female	60	163	80476	40236
020	34	Female	61	172	93272	46640
021	26	Female	58	173	91248	45600
022	24	Female	56	170	107988	53988
023	31	Female	56	160	110216	54922
024	30	Female	57	161	88268	44114
025	25	Female	45	167	8840	4432
026	26	Female	40	168	87296	43648

TABLE 1. *(Continued.)* **Anthropometry and demographics information of 30 left femur images.**

027	28	Female	46	166	123404	61698
028	30	Female	61	159	86020	43024
029	38	Female	65	158	102688	51344
030	40	Female	60	163	89912	44960

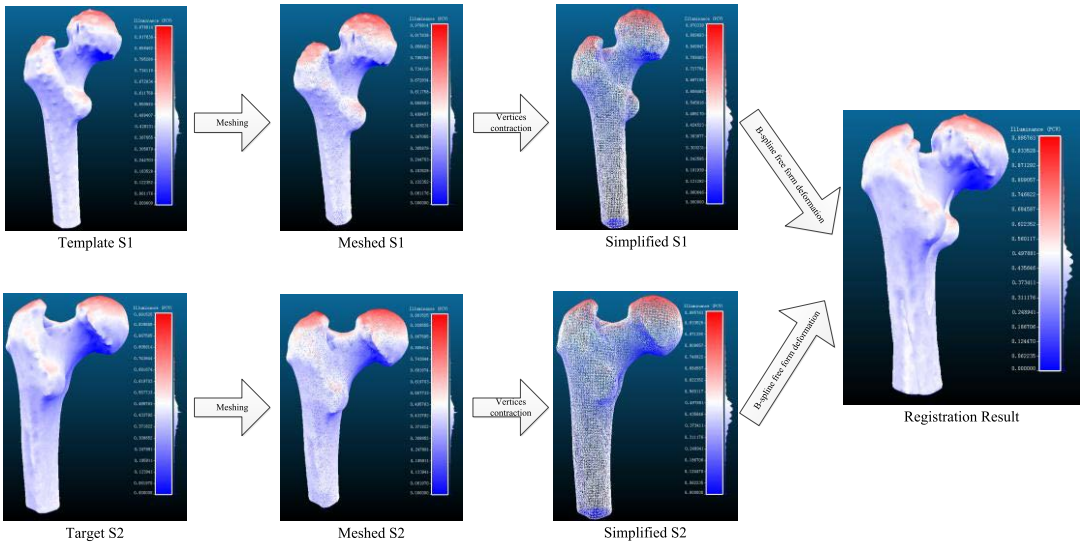

FIGURE 7. Visualization Registration process between template specimen S_1 and target specimen S_2.

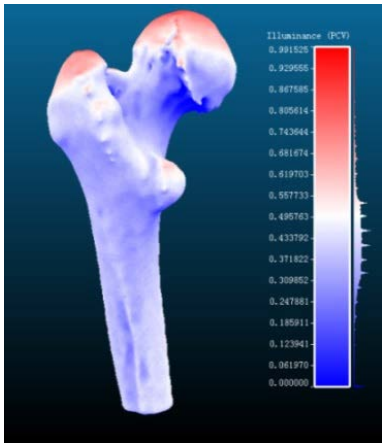

FIGURE 8. Patient-specific anatomical structure model.

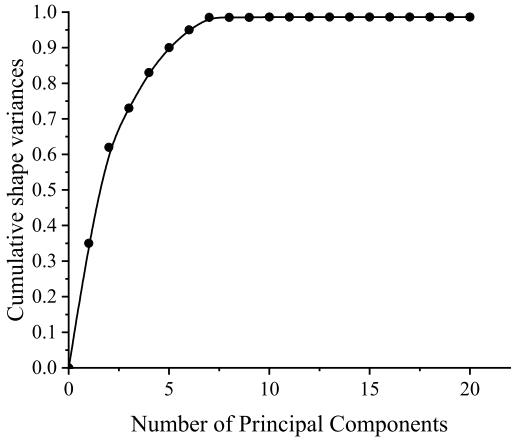

FIGURE 9. The percentage of represented deformation models according to the principal components.

The vertices contraction is applied to S_1', S_1'' is generated. The visualization of S_1'' is shown in Figure 6. The numbers of triangle surfaces and vertices are reduced from 102,080 to 13,478 and from 51,042 to 6,726, respectively. Note that the same procedure of vertices contraction is applied to the remaining specimens $\{S_2, S_3 \ldots S_{30}\}$.

Then, the registration is conducted by using the correspondence that is constructed by using S_1'' and S_2''. The overall registration process is depicted in Figure 7. The principal component analysis is applied to generate the final patient-specific anatomical structure model. Figure 8 depicts the patient-specific anatomical structure model.

For 30 left femurs, the first seven principal components are empirically selected to represent the 98.5% deformation models as shown in Figure 9.

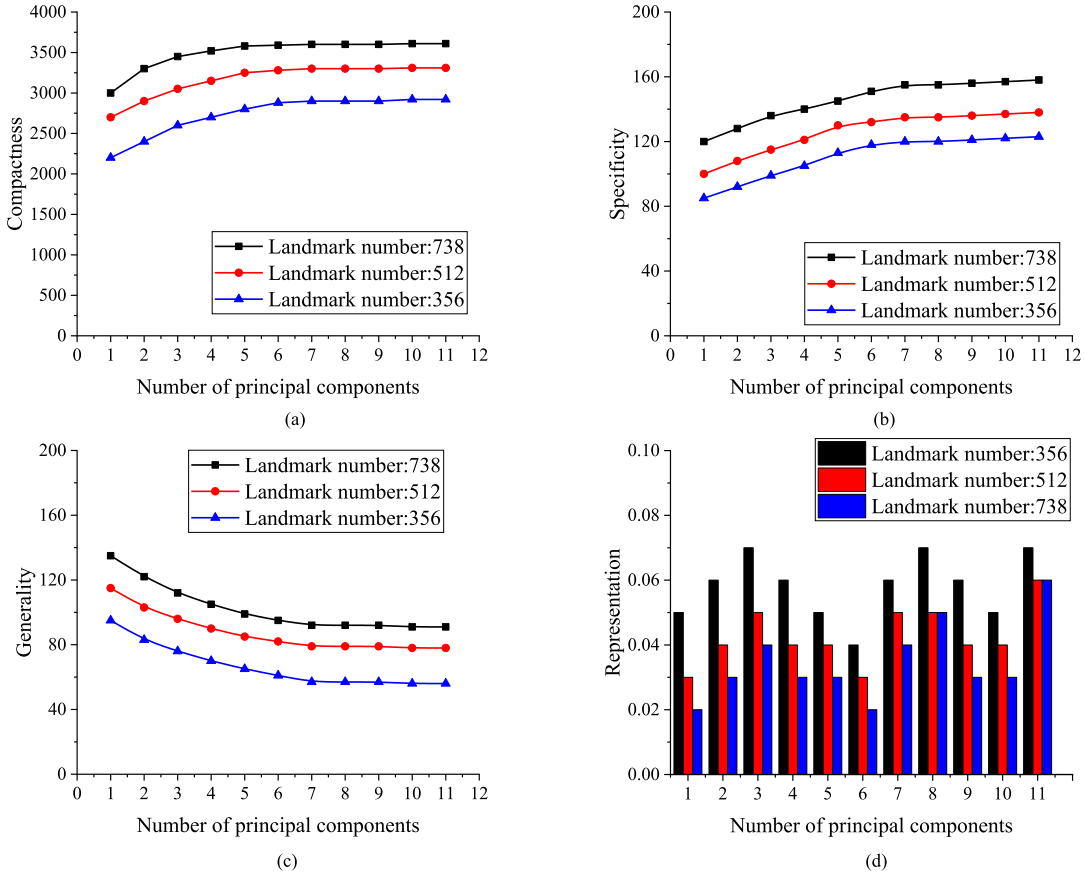

FIGURE 10. Performance comparison of models with different number of landmark points. (a) Performance of Compactness. (b) Performance of Specificity. (c) Performance of Generality. (d) Performance of Representation.

TABLE 2. Comparative of mesh simplification ability of three methods.

ID	Before Simplification		Vertices Contraction		QECD		MCEC	
	surfaces	vertices	surfaces	vertices	surfaces	vertices	surfaces	vertices
001	105694	53149	15681	7680	52847	26619	345	255
002	105694	53149	15047	7421	52848	26622	\	\

In Figure 9, the percentage of the cumulative deformation models increases as the number of principal components increases. After seven principal components, the percentage of cumulative deformation models does not increase over 98.5%. It manifests that the deformation models can be accurately approximated by the first seven principal components.

B. APPROPRIATE LANDMARK POINTS SELECTION

More landmark points can construct a more accurate model while fewer landmark points construct a simpler model. Different numbers of landmark points are compared in this section: 738, 512, and 356 landmark points in terms of compactness, specificity, generality and representation error. The results are shown in Figure 10 (a) $\sim$ (d).

In Figure 10, the scale number of principal components represents the number of the entire deformed models that we want the first several principal components to represent. The normalized cross-correlation (NCC) is used for measuring the similarity. Also, the representation error $E_{representation}$ is $E_{representation} = \frac{1}{L}\sum_{l\in L} Hausdorff\ (p, l)$, where $Hausdorff\ (p, l)$ indicates Hausdorff distance of point p and landmark point l. P and L are the numbers of points and landmark points in the image.

From Figure 10, fewer landmark points provide better performance in terms of compactness, specificity and generality.

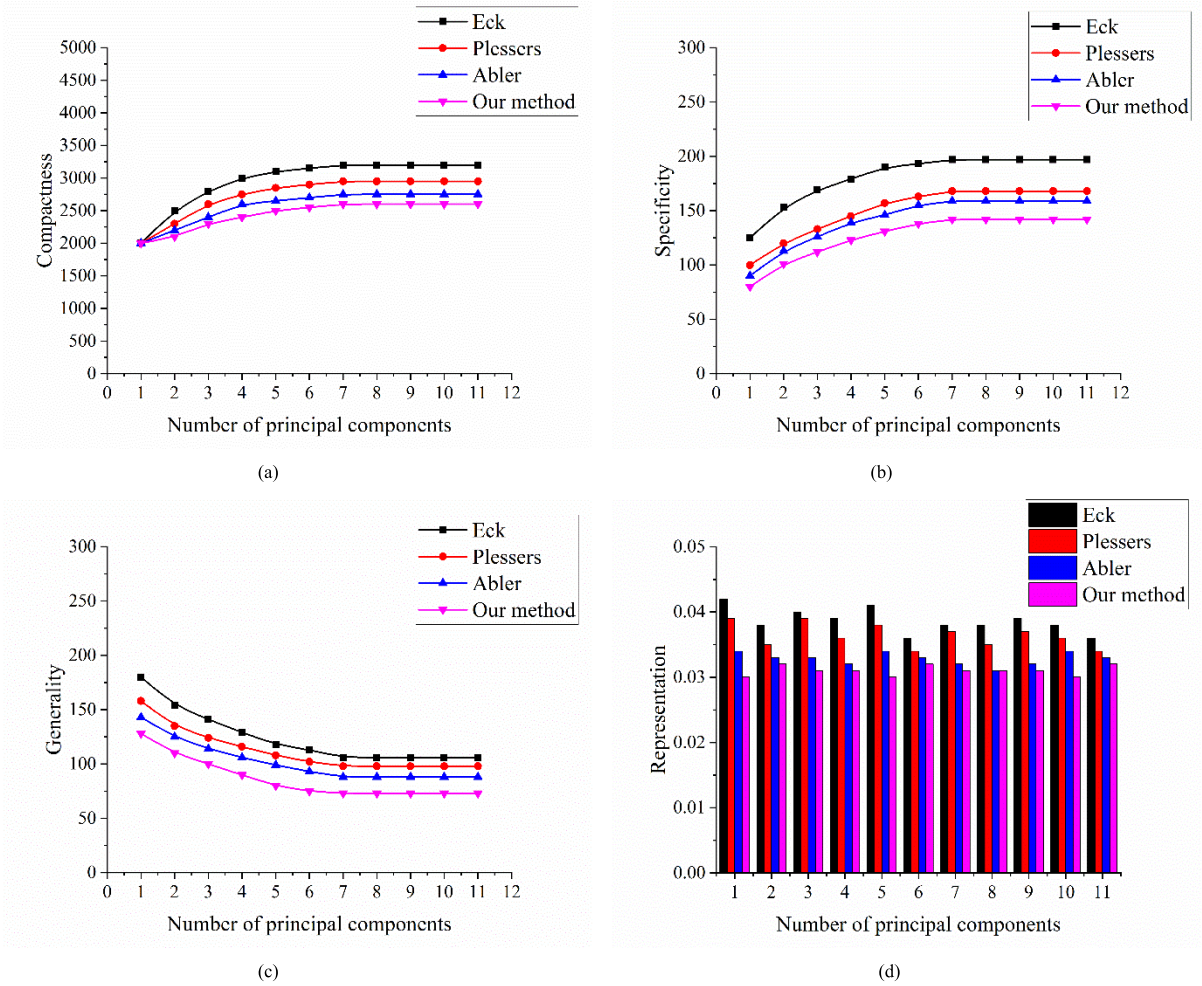

FIGURE 11. Performance evaluation with other methods. (a) Performance of Compactness. (b) Performance of Specificity. (c) Performance of Generality. (d) Performance of Representation.

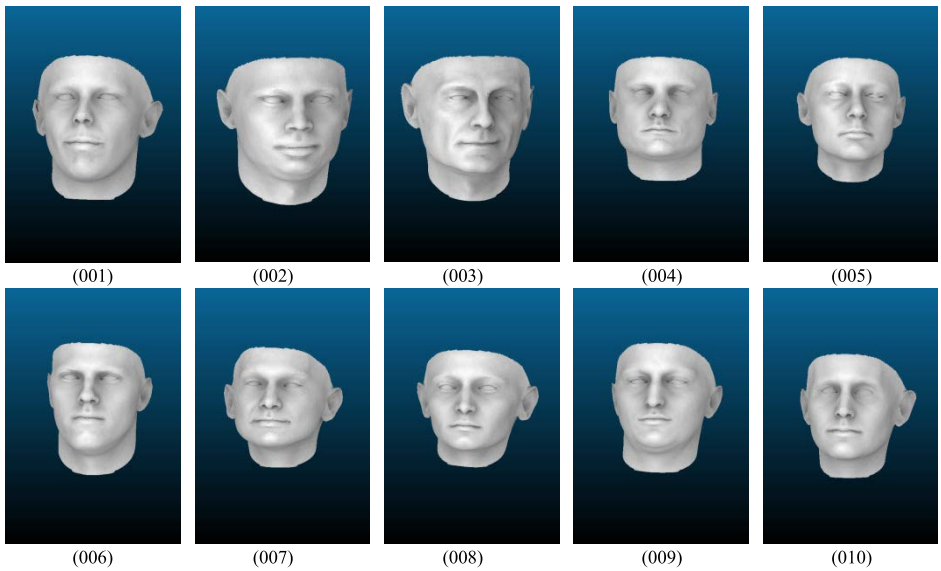

FIGURE 12. Visualization results of 10 groups of face data.

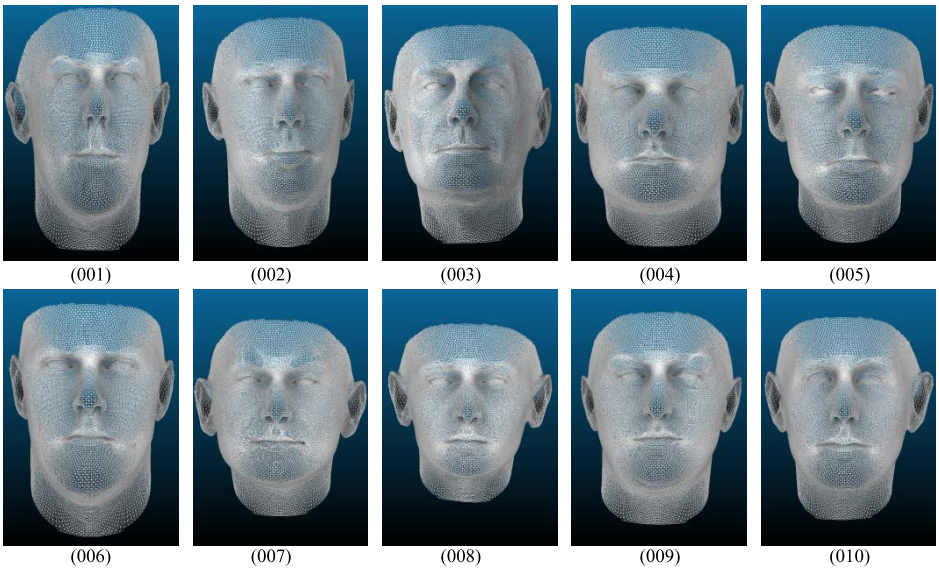

FIGURE 13. Meshing results of 10 groups of face data.

In contrast, a large number of landmark points provide less model representation error. After considering four metrics, the proper number of landmark points is selected as 512.

C. PERFORMANCE EVALUATION OF THE PROPOSED METHOD

To evaluate the performance of our method, we compare our method with Eck, Abler and Plessers. We regard compactness, specificity, generality and representation error as evaluation indicators.

The comparison results are shown in Figure 11. From Figure 11, we can see that our method has the best compactness, specificity, generality and the smallest representation error. Overall, the experimental results prove that the proposed method can effectively construct a patient-specific anatomical structure model and has better performance than Eck, Abler and Plessers.

D. ANALYSIS OF MESH SIMPLIFICATION ABILITY

In order to further verify the mesh simplification ability of the vertices contraction strategy proposed in this paper, we compare the vertices contraction with MCEC and the QECD respectively. In the process of analyzing the mesh simplification ability, we use 10 groups of 3D face data published by Basel University for verification. The simulation software and hardware environment for face data verification are CPU Intel(R) Core(TM) i5-2430M 2.40 GHz, RAM 8GB, 64-bit Scalismolab, Visual Studio2015, ITK4.12, VTK6.3, Qt5.9 and 64-bit Windows7 SP1. The visualization results of 10 groups of face data are shown in Figure 12.

After obtaining the visualization results of the face data, we arbitrarily select 001 of the face data as the template specimen and mesh it with triangles, and then mesh the remaining 9 target specimens. The visualization results of 10 face data after meshing are shown in Figure 13.

Statistics show that after 10 face data are meshed, the number of triangle surfaces is 105694, and the number of triangle vertices is 53149. After obtaining the meshing results of the face data, we use vertices contraction, QECD and MCEC to simplify the mesh, and the results are shown in Figure 14.

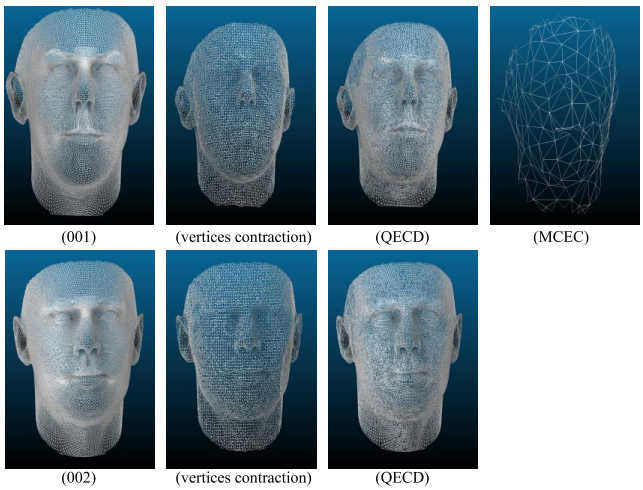

FIGURE 14. Mesh simplification results of three methods.

The first row of Figure 14 is to perform vertices contraction, QECD and MCEC on the meshing results of template specimen 001. The second row is the meshing results of the target specimen 002 with vertices contraction and QECD. Because the MCEC is severely distorted, the simplified result of 002 under the MCEC cannot be displayed.

It can be seen from Figure 14 that both vertices contraction and QECD can reduce the number of triangular surfaces, and ensure that the specimen is not distorted. Meanwhile, we can clearly observe that the effect of vertices contraction is significantly better than that of QECD. In addition, although

MCEC can greatly reduce the number of triangular surfaces and vertices, serious distortion would occur. In order to analyze the mesh simplification ability of the three methods more intuitively, we perform a statistical analysis on the changes of the number of triangle surfaces and the number of vertices before and after the simplification in Figure 14, and the results are shown in Table 2.

It can be seen from Table 2 that the number of triangle surfaces of template specimen 001 is reduced to 90013 and the number of triangle vertices is reduced to 45469 after vertices contraction. Furthermore, the number of triangle surfaces is reduced to 52847 and the number of triangle vertices is reduced to 26530 after QECD. For the target specimen 002, the number of triangle surfaces and the number of vertices are reduced to 90647 and 45728 respectively after vertices contraction. At the same time, the number of triangle surfaces and the number of vertices are reduced to 52846 and 26527 respectively after QECD.

Therefore, we can conclude that vertices contraction has batter mesh simplification effect than QECD and MCEC.

IV. DISCUSSIONS

Different from the compared methods, our method regards the statistical shape model as the basis. By introducing the vertices contraction strategy in the phase of establishing correspondence between the template specimen and the target specimens, the number of mesh vertices of the training specimen is effectively reduced, thereby the amount of calculation is reduced. Furthermore, B-spline free-form deformation for registration is introduced. By minimizing the objective function, the anatomical structure model with better performance can be effectively constructed. Thereafter, the first 20 principal components of the entire deformation models are analyzed that the deformation models can be accurately approximated by the first seven principal components.

To verify the effectiveness of our method, 30 sets of left femurs of the pelvis are used as training data for validation. By analyzing the experimental results, when the vertices contraction strategy is introduced, the numbers of triangle surfaces and vertices are reduced from 102,080 to 13,478 and from 51,042 to 6,726. Meanwhile, after vertices contraction, the left femur is visualized. It can be seen from the visualization results that the vertices contraction strategy can effectively reduce the number of mesh vertices of the training specimen without distortion. Furthermore, we compared our method with the other methods, and their compactness, specificity, generality and representation are evaluated. The results demonstrate that our method has better performance.

V. CONCLUSION

We propose a novel method to construct a patient-specific anatomical structure model based on statistical shape model. In the method, the number of vertices in the triangle meshes is effectively reduced by using the vertices contraction strategy. Then, improved B-spline free-form deformation is introduced to establish the correspondence. Finally, the patient-specific anatomical structure model is generated by principal component analysis. The experimental results show that our method can effectively construct a patient-specific anatomical structure model.

REFERENCES

[1] C. J. F. Reyneke, M. Luthi, V. Burdin, T. S. Douglas, T. Vetter, and T. E. M. Mutsvangwa, "Review of 2-D/3-D reconstruction using statistical shape and intensity models and X-ray image synthesis: Toward a unified framework," *IEEE Rev. Biomed. Eng.*, vol. 12, pp. 269–286, 2019.

[2] N. Sarkalkan, H. Weinans, and A. A. Zadpoor, "Statistical shape and appearance models of bones," *Bone*, vol. 60, pp. 129–140, Mar. 2014.

[3] N. Ravikumar, A. Gooya, S. Çimen, A. F. Frangi, and Z. A. Taylor, "Group-wise similarity registration of point sets using student's t-mixture model for statistical shape models," *Med. Image Anal.*, vol. 44, pp. 156–176, Feb. 2018.

[4] A. L. Clouthier, C. R. Smith, M. F. Vignos, D. G. Thelen, K. J. Deluzio, and M. J. Rainbow, "The effect of articular geometry features identified using statistical shape modelling on knee biomechanics," *Med. Eng. Phys.*, vol. 66, pp. 47–55, Apr. 2019.

[5] M. A. Fuessinger, S. Schwarz, J. Neubauer, C.-P. Cornelius, M. Gass, P. Poxleitner, R. Zimmerer, M. C. Metzger, and S. Schlager, "Virtual reconstruction of bilateral midfacial defects by using statistical shape modeling," *J. Cranio-Maxillofacial Surg.*, vol. 47, no. 7, pp. 1054–1059, Jul. 2019.

[6] J. F. M. Hollenbeck, C. M. Cain, J. A. Fattor, P. J. Rullkoetter, and P. J. Laz, "Statistical shape modeling characterizes three-dimensional shape and alignment variability in the lumbar spine," *J. Biomech.*, vol. 69, pp. 146–155, Mar. 2018.

[7] J. D. Shirk, L. Kwan, and C. Saigal, "The use of 3-dimensional, virtual reality models for surgical planning of robotic partial nephrectomy," *Urology*, vol. 125, pp. 92–97, Mar. 2019.

[8] V. Sindhu and S. Soundarapandian, "Three-dimensional modelling of femur bone using various scanning systems for modelling of knee implant and virtual aid of surgical planning," *Measurement*, vol. 141, pp. 190–208, Jul. 2019.

[9] T. Liu, S. Qin, D. Zou, W. Song, and J. Teng, "Mesoscopic modeling method of concrete based on statistical analysis of CT images," *Construction Building Mater.*, vol. 192, pp. 429–441, Dec. 2018.

[10] J. R. Meakin, S. J. Hopkins, and A. Clarke, "*In vivo* assessment of thoracic vertebral shape from MRI data using a shape model," *Spine Deformity*, vol. 7, no. 4, pp. 517–524, Jul. 2019.

[11] A. Kelemen, G. Szekely, and G. Gerig, "Elastic model-based segmentation of 3-D neuroradiological data sets," *IEEE Trans. Med. Imag.*, vol. 18, no. 10, pp. 828–839, Oct. 1999.

[12] R. H. Davies, C. J. Twining, T. F. Cootes, J. C. Waterton, and C. J. Taylor, "A minimum description length approach to statistical shape modeling," *IEEE Trans. Med. Imag.*, vol. 21, no. 5, pp. 525–537, May 2002.

[13] R. H. Davies, *Learning Shape: Optimal Models for Analysing Natural Variability*. Manchester, U.K.: Univ. Manchester Manchester, 2002.

[14] P. Dalal and S. Wang, "Landmark sliding for 3D shape correspondence," in *Intelligent Data Analysis for Real-Life Applications: Theory and Practice*. PA, USA: IGI Global, 2012, pp. 57–71.

[15] D. C. Barratt, C. S. K. Chan, P. J. Edwards, G. P. Penney, M. Slomczykowski, T. J. Carter, and D. J. Hawkes, "Instantiation and registration of statistical shape models of the femur and pelvis using 3D ultrasound imaging," *Med. Image Anal.*, vol. 12, no. 3, pp. 358–374, Jun. 2008.

[16] S. Eck, S. Wörz, K. Müller-Ott, M. Hahn, A. Biesdorf, G. Schotta, K. Rippe, and K. Rohr, "A spherical harmonics intensity model for 3D segmentation and 3D shape analysis of heterochromatin foci," *Med. Image Anal.*, vol. 32, pp. 18–31, Aug. 2016.

[17] D. Abler, S. Berger, A. Terrier, F. Becce, A. Farron, and P. Büchler, "A statistical shape model to predict the premorbid glenoid cavity," *J. Shoulder Elbow Surg.*, vol. 27, no. 10, pp. 1800–1808, Oct. 2018.

[18] K. Plessers, P. V. Berghe, C. Van Dijck, R. Wirix-Speetjens, P. Debeer, I. Jonkers, and J. Vander Sloten, "Virtual reconstruction of glenoid bone defects using a statistical shape model," *J. Shoulder Elbow Surg.*, vol. 27, no. 1, pp. 160–166, Jan. 2018.

[19] Z. Gao, X. Liu, S. Qi, W. Wu, W. K. Hau, and H. Zhang, "Automatic segmentation of coronary tree in CT angiography images," *Int. J. Adapt. Control Signal Process.*, vol. 33, no. 8, pp. 1239–1247, Aug. 2019.
[20] J. S., B. T. A., and R. Rangasami, "A novel segmentation of cochlear nerve using region growing algorithm," *Biomed. Signal Process. Control*, vol. 39, pp. 117–129, Jan. 2018.
[21] J. Wu, D. Zhang, X. Yi, F. Luo, and T. Zhang, "Improved marching cubes algorithm for 3D multi-slice spiral computed tomography in the diagnosis of bone and joint diseases," *J. Med. Imag. Health Informat.*, vol. 9, no. 5, pp. 962–968, Jun. 2019.
[22] H. Wang and B. Fei, "Nonrigid point registration for 2D curves and 3D surfaces and its various applications," *Phys. Med. Biol.*, vol. 58, no. 12, pp. 4315–4330, Jun. 2013.
[23] H. Henseler, B. Khambay, X. Ju, A. Ayoub, and A. K. Ray, "Landmark-based statistical Procrustes analysis in the examination of breast shape and symmetry," *Handchirurgie, Mikrochirurgie, Plastische Chirurgi*, vol. 46, no. 6, pp. 342–349, Jun. 2014.
[24] R. Haq, J. Cates, D. A. Besachio, and M. A. Audette, "Statistical shape model construction of lumbar vertebrae and intervertebral discs in segmentation for discectomy surgery simulation," in *Proc. Int. Workshop Challenge Comput. Methods Clin. Appl. Spine Imag.*, 2015, pp. 85–96.
[25] T. Mutsvangwa, V. Burdin, C. Schwartz, and C. Roux, "An automated statistical shape model developmental pipeline: Application to the human scapula and humerus," *IEEE Trans. Biomed. Eng.*, vol. 62, no. 4, pp. 1098–1107, Apr. 2015.
[26] G. Zheng, Z.-C. Li, and J. Gu, "Evaluation of 3D correspondence methods for building point distribution models of the kidney," in *Proc. 5th Int. Conf. Biomed. Eng. Informat.*, Oct. 2012, pp. 637–640.

ZHUYE XU received the Ph.D. degree from the Lanzhou University of Technology, in 2021. He is currently a Teacher with Lanzhou Jiaotong University. His main research interest includes medical image processing.

XIAOQIANG ZHAO received the Ph.D. degree from Zhejiang University, in 2006. He is currently a Professor and a Ph.D. Supervisor with the Lanzhou University of Technology. His main research interests include process monitoring and fault diagnosis, and medical image processing.